UCLA

Title

Observing crystal nucleation in four dimensions using atomic electron tomography

Authors

Zhou, Jihan

Yang, Yongsoo

Yang, Yao

et al.

Peer reviewed

Capturing nucleation at 4D atomic resolution

Jihan Zhou[1*], Yongsoo Yang[1*†], Yao Yang[1], Dennis S. Kim[1], Andrew Yuan[1], Xuezeng Tian[1], Colin Ophus[2], Fan Sun[3], Andreas K. Schmid[2], Michael Nathanson[4], Hendrik Heinz[4], Qi An[5], Hao Zeng[3], Peter Ercius[2] & Jianwei Miao[1]

[1]*Department of Physics & Astronomy and California NanoSystems Institute, University of California, Los Angeles, CA 90095, USA. [2]National Center for Electron Microscopy, Molecular Foundry, Lawrence Berkeley National Laboratory, Berkeley, CA 94720, USA. [3]Department of Physics, University at Buffalo, the State University of New York, Buffalo, NY 14260, USA. [4]Department of Chemical and Biological Engineering, University of Colorado at Boulder, Boulder, CO 80309, USA. [5]Chemical and Materials Engineering, University of Nevada, Reno, NV 89557-0388, USA.*

[*]These authors contributed equally to this work. [†]Present address: Department of Physics, Korea Advanced Institute of Science and Technology, Daejeon 34141, Korea.

Nucleation plays a critical role in many physical and biological phenomena ranging from crystallization, melting and evaporation to the formation of clouds and the initiation of neurodegenerative diseases[1-3]. However, nucleation is a challenging process to study in experiments especially in the early stage when several atoms/molecules start to form a new phase from its parent phase. Over the years, a number of experimental and computational methods have been used to investigate nucleation processes[4-17], but it remains unachievable to experimentally determine the 3D atomic structure and dynamics of early stage nuclei. Here, we develop 4D atomic electron tomography (AET) to study early stage nucleation at atomic resolution. Using FePt nanoparticles as a model system, we reveal that early stage nuclei are irregularly shaped, each has a core of one to a few atoms

with the maximum order parameter, and the order parameter gradient points from the core to the boundary of the nucleus. We capture the structure and dynamics of the same nuclei undergoing growth, fluctuation, dissolution, merging and/or division, which are regulated by the order parameter distribution and its gradient. These experimental observations are corroborated by molecular dynamics simulations of heterogeneous and homogeneous nucleation in liquid-solid phase transitions of Pt. Our experimental and molecular dynamics results differ from classical nucleation theory (CNT)[1,2,18], indicating a theory beyond CNT is needed to describe early stage nucleation at the atomic scale. Looking forward, we anticipate that 4D AET opens the door to study many fundamental problems in materials science, nanoscience, condensed matter physics and chemistry such as phase transition, atomic diffusion, grain boundary dynamics, interface motion, defect dynamics and surface reconstruction with 4D atomic resolution.

AET is a powerful method to determine the 3D atomic structure of materials without the assumption of crystallinity[19] and has been applied to study dislocations, stacking faults, grain boundaries, atomic displacement, strain tensor, chemical order/disorder and point defects with unprecedented 3D detail[20-26]. But all of these studies were of static structures. To probe the 4D atomic structure of early stage nucleation, we have tracked the same nuclei at different times and applied AET to determine their 3D atomic coordinates and species at each time (Methods). We used FePt nanoparticles as a model system because binary alloys have been widely used to study phase transitions[2] and FePt is a very promising material for next generation magnetic recording media[25,27]. As-synthesized FePt nanoparticles form a chemically disordered face-centred cubic (fcc) structure (A1 phase)[27]. With annealing, the A1 phase

undergoes a solid-solid transition to an ordered face-centred tetragonal (L1$_0$) phase or a chemically ordered fcc (L1$_2$) phase[25,27]. To validate 4D AET, we first performed a consistency check experiment of FePt nanoparticles undergoing phase transitions. We annealed the nanoparticles at 520°C for 9 minutes in vacuum and acquired two independent, sequential tilt series of an FePt nanoparticle (named particle 1) with a scanning transmission electron microscope[28] (Methods and Extended Data Table 1). After reconstructing the two data sets using a GENeralized Fourier Iterative REconstruction algorithm (GENFIRE)[25,29], we located and identified the 3D coordinates of all individual Fe and Pt atoms (Methods). Extended Data Figs. 1a-f show the 3D atomic models obtained from the two independent measurements of the same nanoparticle. By comparing their 3D atomic coordinates and species, we confirmed that 95.4% of atoms are consistent between the two models and the precision of our 3D atomic structure determination method is 26 pm (Extended Data Fig. 1g).

Next, we trapped the same FePt nanoparticles at different annealing times and acquired a tilt series at each time (Methods). By applying the same reconstruction, atom tracing, atom identification and refinement procedures, we obtained a 3D atomic model for each tilt series. Figures 1a-c show the atomic models of the same nanoparticle (named particle 2) with an accumulated annealing time of 9, 16 and 26 minutes, respectively. We observed that the total number of atoms in the nanoparticle was slightly changed at the three annealing times (Extended Data Table 1). This was caused by atomic diffusion between nanoparticles during annealing, as confirmed by an energy-dispersive x-ray spectroscopy experiment (Extended Data Fig. 2). The overall 3D shape of the nanoparticle was similar between 9 and 16 minutes of annealing, but changed from 16 to 26 minutes. A fraction of the surface and sub-surface atoms were re-arranged

to form $L1_0$ phases, but the Pt-rich core of the nanoparticle remained the same (Figs. 1d-f), which is evident by comparing the same internal atomic layers along the [010] direction (Figs. 1g-i). These experimental observations can be explained by vacancy-mediated atomic diffusion during annealing as it is energetically more favourable to create vacancies on or near the surface than in the core of the nanoparticle[2]. Extended Data Fig. 3 shows the 3D atomic models of another FePt nanoparticle (named particle 3) with an accumulated annealing time of 9 and 16 minutes, showing similar results to particle 2 (Fig. 1).

The annealed FePt nanoparticles consist of A1, $L1_0$, and $L1_2$ phases, which were quantified by the short-range order parameter (termed the order parameter for simplicity, Methods). Using the order parameter, we identified nuclei with the $L1_0$, Fe-rich A1, Pt-rich A1, Fe-rich $L1_2$ and Pt-rich $L1_2$ phases in these nanoparticles, where we define a nucleus with a minimum of 13 atoms (the centre atom plus its 12 nearest fcc neighbours). As the $L1_0$ phase is more abundant than the $L1_2$ phase in the nanoparticles and also technologically more important[25,27], we focused on the analysis of the $L1_0$ phase nuclei in this work. Careful examination of all the nuclei indicates that each early stage nucleus has a core of one to a few atoms with the maximum order parameter. To locate the nucleation sites, we searched for the cores of all the $L1_0$ phase nuclei inside the nanoparticles. The distribution of the nucleation sites in particle 1 is in agreement between two independent measurements (Extended Data Fig. 4a-c). Figure 2a-d and Extended Data Fig. 4d-f show the evolution of the nucleation sites as a function of the annealing time in particles 2 and 3, respectively. If the core of a nucleus is within one unit cell distance (3.87 Å) from the surface, we define it as a surface site. Otherwise, it is defined as a sub-surface site. Most nucleation sites in particles 2 and 3 are located on

the facets, edges or corners, where the <100> and <111> facets are shown in green and magenta colour, respectively. Compared to particles 2 and 3, particle 1 has more nucleation sites at the sub-surface, because many of its nuclei are relatively large and extends further into the nanoparticle. All our observations confirm that the nucleation is heterogeneous, which is energetically more favourable than homogeneous nucleation[1,2].

To probe nucleation dynamics, we tracked the same nuclei in each particle at different annealing times (termed common nuclei). By quantitatively comparing all the nuclei of the same particle at different annealing times, we identified 33 and 25 common nuclei in particles 2 and 3, respectively (Methods). As each atom is associated with an order parameter, we define the effective number of atoms by summing up the order parameters in each nucleus. We found that the order parameter of the nucleus core (α_0) is correlated with the effective number of atoms (Extended Data Fig. 4g). Based on the effective number of atoms, we divided the common nuclei into three groups: growing, fluctuating and dissolving nuclei (Methods). Figure 3 shows five growing, fluctuating and dissolving nuclei in particle 2, where each nucleus is represented by an atomic model and a 3D contour map with an order parameter equal to 0.7 (red), 0.5 (purple) and 0.3 (light blue). Particle 2 has 14 growing, 14 fluctuating and 5 dissolving nuclei (Fig. 3, Extended Data Figs. 5, 6, and 7) and particle 3 has 16 growing and 9 dissolving nuclei. Among these common nuclei, we also observed merging and dividing nuclei, shown in Fig. 3g-l, Extended Data Figs. 5b-d and 6e.

Next, we analysed the order parameter distribution in the common nuclei as a function of the annealing time. Figure 4a-c show the order parameter distribution of a growing nucleus in particle 2 (Fig. 3a-c) along the [110], [111] directions and with radial average, respectively, where the order parameter increases with the increment of

the annealing time. A generalized Gaussian distribution was used to fit the order parameter distribution,

$$\alpha(r) = \alpha_0 e^{\left(-\frac{r}{\lambda}\right)^{\beta}},\qquad(1)$$

where α_0, λ and β are the fitting parameters. Figure 4a-c and Extended Data Fig. 7e-m show the fit of the equation to the measured order parameter of several representative nuclei, indicating equation (1) (solid curves) is in good agreement with the experimental data (dots). In addition to the order parameter, we found that the order parameter gradient (OPG) also plays an important role in nucleation dynamics, which points from the core of each nucleus to its boundary. Figure 4d-f shows the 3D OPG distribution of the growing nucleus at three different annealing times. As the nucleus grows, the OPG spreads out further along the radial direction. To perform a quantitative analysis, we summed up the OPG inside each nucleus, which we term the effective surface area of the nucleus as it has the same dimension as area. Figure 2e shows a plot of the effective surface area vs. the effective number of atoms for all the nuclei in particles 2 and 3. The dissolving nuclei are clustered near the lower left corner of the plot, while both small and large nuclei can fluctuate as a function of time.

Our experimental study of early stage nucleation reveals three observations that cannot be explained by CNT[1,2,18]. First, early stage nuclei are anisotropic, as characterized with sphericity[30], a measure of how closely the shape of a 3D object approaches a perfect sphere. Extended Data Fig. 4h shows the sphericity of the nuclei as a function of the effective number of atoms, where the majority of the nuclei have a sphericity between 0.5 and 0.9 (with 1.0 as a perfect sphere). The nonspherical shape of early stage nuclei is caused by geometrical constraint, local inhomogeneity and anisotropy of the interfacial tension. This result is also consistent with the previous

experimental observation of the nucleus shape of anisotropic molecules using atomic force microscopy[5]. Second, each nucleus has a core of one to a few atoms with the maximum order parameter and the OPG points from the core to the boundary of the nucleus (Fig. 4d-f and Extended Data Fig. 4g), resulting in a diffuse interface between the nucleus and its parent phase. Third, we observed some common nuclei undergoing growth, fluctuation, dissolution, merging and/or division (Fig. 3 and Extended Data Figs. 5-7), which are regulated by the order parameter distribution and its gradient. Each order parameter distribution and its gradient represent a metastable state and a nucleus can fluctuate between two metastable states. Numerous such fluctuating nuclei were observed in our experimental data (Fig. 3d-l and Extended Data Fig. 6).

To further corroborate our experimental observations, we performed MD simulations of heterogeneous and homogeneous nucleation in liquid-solid phase transitions. The simulations were carried out using the large-scale atomic/molecular massively parallel simulator (LAMMPS)[31]. To enable cross-validation of the results, for heterogeneous nucleation we applied both the embedded-atom method potential and the interface force field to simulate two Pt liquid nanodroplets above the melting temperature (Methods). We then lowered the temperature to investigate early stage nucleation in crystallization. After analysing all the nuclei with the average local bond order parameter[32,33] (Methods), we found most nuclei are located on or near the surface of the two nanoparticles and each nucleus has a core of one to a few atoms with the maximum order parameter. Using the same criterion as the experimental data, we identified the common nuclei at different times and observed nucleation dynamics including growth, fluctuation, merging, division and dissolution. Figure 5a-d and Extended Data Fig. 8a-d show four representative growing, fluctuating, merging,

dividing and dissolving nuclei for the embedded-atom method and the interface force field, respectively. The order parameter distributions of these nuclei with radial distance are shown in Fig. 5e-h and Extended Data Fig. 8e-h, indicating that nucleation dynamics is regulated by the order parameter distribution and its gradient. For homogeneous nucleation, we used the embedded-atom method potential with periodic boundary conditions to simulate a bulk Pt system undergoing liquid-solid phase transitions (Methods). Extended Data Fig. 9 shows four representative growing, fluctuating, merging, dividing and dissolving nuclei and their order parameter distributions. All the MD simulation results of heterogeneous and homogeneous nucleation are consistent with our experimental observations.

In conclusion, we developed 4D AET to study the structure and dynamics of nucleation at atomic resolution. We found that early stage nuclei are nonspherical, each nucleus has a core of one to a few atoms with the maximum order parameter, and the OPG points from the core to the boundary. We captured the same nuclei undergoing growth, fluctuation, dissolution, merging and/or division. We further validated these experimental observations by performing MD simulations of heterogeneous and homogeneous nucleation in liquid-solid phase transitions of Pt. Both our experimental and MD results are inconsistent with CNT, showing the need of a beyond CNT model to explain early stage nucleation at the atomic scale. Furthermore, as $L1_0$ FePt is a material with a great technological potential, our experimental results on the early stage nucleation of the $L1_0$ FePt phase could expand our understanding of the critical conditions and requirements to make superior magnetic recording media and catalysts[25,27]. Finally, all the seven experimental atomic models with 3D coordinates reported here have been deposited in the Materials Data Bank, an open database to serve

the physical science community, which is analogous to the Protein Data Bank for the biological and life science communities. These experimentally measured coordinates can be used as direct input for density functional theory calculations and MD simulations of material properties[25,26], which is anticipated to open a new window to study the structure-property relationships of materials with 4D atomic resolution.

References

1. Kelton, K. F. & Greer, A. L. *Nucleation in Condensed Matter: Applications in Materials and Biology*. (Pergamon, 2010).

2. Porter, D. A., Easterling, K. E. & Sherif, M. Y. *Phase transformations in metals and alloys*. (CRC Press, 2009).

3. Jucker, M. & Walker, L. C. Self-propagation of pathogenic protein aggregates in neurodegenerative diseases. *Nature* **501**, 45–51 (2013).

4. Wolde, P. R. ten & Frenkel, D. Enhancement of Protein Crystal Nucleation by Critical Density Fluctuations. *Science* **277,** 1975–1978 (1997).

5. Yau, S.-T. & Vekilov, P. G. Quasi-planar nucleus structure in apoferritin crystallization. *Nature* **406**, 494-497 (2000).

6. Auer, S. & Frenkel, D. Prediction of absolute crystal-nucleation rate in hard-sphere colloids. *Nature* **409,** 1020–1023 (2001).

7. Gasser, U., Weeks, E. R., Schofield, A., Pusey, P. N. & Weitz, D. A. Real-Space Imaging of Nucleation and Growth in Colloidal Crystallization. *Science* **292,** 258–262 (2001).

8. Anderson, V. J. & Lekkerkerker, H. N. W. Insights into phase transition kinetics from colloid science. *Nature* **416,** 811–815 (2002).

9. Kelton, K. F. *et al.* First X-Ray Scattering Studies on Electrostatically Levitated Metallic Liquids: Demonstrated Influence of Local Icosahedral Order on the Nucleation Barrier. *Phys. Rev. Lett.* **90,** 195504 (2003).

10. Merikanto, J., Zapadinsky, E., Lauri, A. & Vehkamäki, H. Origin of the Failure of Classical Nucleation Theory: Incorrect Description of the Smallest Clusters. *Phys. Rev. Lett.* **98,** 145702 (2007).

11. Gebauer, D., Völkel, A. & Cölfen, H. Stable Prenucleation Calcium Carbonate Clusters. *Science* **322,** 1819–1822 (2008).

12. Pouget, E. M. *et al.* The Initial Stages of Template-Controlled $CaCO_3$ Formation Revealed by Cryo-TEM. *Science* **323,** 1455–1458 (2009).

13. Nielsen, M. H., Aloni, S. & De Yoreo, J. J. In situ TEM imaging of CaCO3 nucleation reveals coexistence of direct and indirect pathways. *Science* **345,** 1158–1162 (2014).

14. Sleutel, M., Lutsko, J., Van Driessche, A. E. S., Durán-Olivencia, M. A. & Maes, D. Observing classical nucleation theory at work by monitoring phase transitions with molecular precision. *Nat. Commun.* **5,** 5598 (2014).

15. Kwon, S. G. *et al.* Heterogeneous nucleation and shape transformation of multicomponent metallic nanostructures. *Nat. Mater.* **14,** 215–223 (2015).

16. Van Driessche, A. E. S. *et al.* Molecular nucleation mechanisms and control strategies for crystal polymorph selection. *Nature* **556,** 89–94 (2018).

17. Chen, J. *et al.* Building two-dimensional materials one row at a time: Avoiding the nucleation barrier. *Science* **362**, 1135–1139 (2018).

18. Vekilov, P. G. Nucleation. *Cryst Growth Des.* **10,** 5007–5019 (2010).

19. Miao, J., Ercius, P. & Billinge, S. J. L. Atomic electron tomography: 3D structures without crystals. *Science* **353,** aaf2157 (2016).

20. Scott, M. C. *et al.* Electron tomography at 2.4-angstrom resolution. *Nature* **483,** 444–447 (2012).

21. Goris, B. *et al.* Three-Dimensional Elemental Mapping at the Atomic Scale in Bimetallic Nanocrystals. *Nano Lett.* **13,** 4236–4241 (2013).

22. Chen, C.-C. *et al.* Three-dimensional imaging of dislocations in a nanoparticle at atomic resolution. *Nature* **496,** 74–77 (2013).

23. Xu, R. *et al.* Three-dimensional coordinates of individual atoms in materials revealed by electron tomography. *Nat. Mater* **14,** 1099–1103 (2015).

24. Haberfehlner, G. *et al.* Formation of bimetallic clusters in superfluid helium nanodroplets analysed by atomic resolution electron tomography. *Nat. Commun.* **6,** 8779 (2015).

25. Yang, Y. *et al.* Deciphering chemical order/disorder and material properties at the single-atom level. *Nature* **542,** 75–79 (2017).

26. Tian, X *et al*. Correlating 3D atomic defects and electronic properties of 2D materials with picometer precision. arXiv:1901.00633 (2019).

27. Sun, S., Murray, C. B., Weller, D., Folks, L. & Moser, A. Monodisperse FePt Nanoparticles and Ferromagnetic FePt Nanocrystal Superlattices. *Science* **287,** 1989–1992 (2000).

28. Pennycook, S. J. & Nellist, P. D. *Scanning Transmission Electron Microscopy: Imaging and Analysis*. (Springer Science & Business Media, 2011).

29. Pryor, A. *et al.* GENFIRE: A generalized Fourier iterative reconstruction algorithm for high-resolution 3D imaging. *Sci. Rep.* **7,** 10409 (2017).

30. Wadell, H. Volume, Shape, and Roundness of Quartz Particles. *J. Geol.* **43,** 250–280 (1935).

31. Plimpton, S. Fast Parallel Algorithms for Short-Range Molecular Dynamics. *J. Comput. Phys.* **117,** 1–19 (1995).

32. Steinhardt, P. J., Nelson, D. R. & Ronchetti, M. Bond-orientational order in liquids and glasses. *Phys. Rev. B* **28,** 784–805 (1983).

33. Lechner, W. & Dellago, C. Accurate determination of crystal structures based on averaged local bond order parameters. *J. Chem. Phys.* **129,** 114707 (2008).

Supplementary Information accompanies the paper on www.nature.com/nature.

Author information The authors declare no competing financial interests. Correspondence and requests for materials should be addressed to J.M. (miao@physics.ucla.edu).
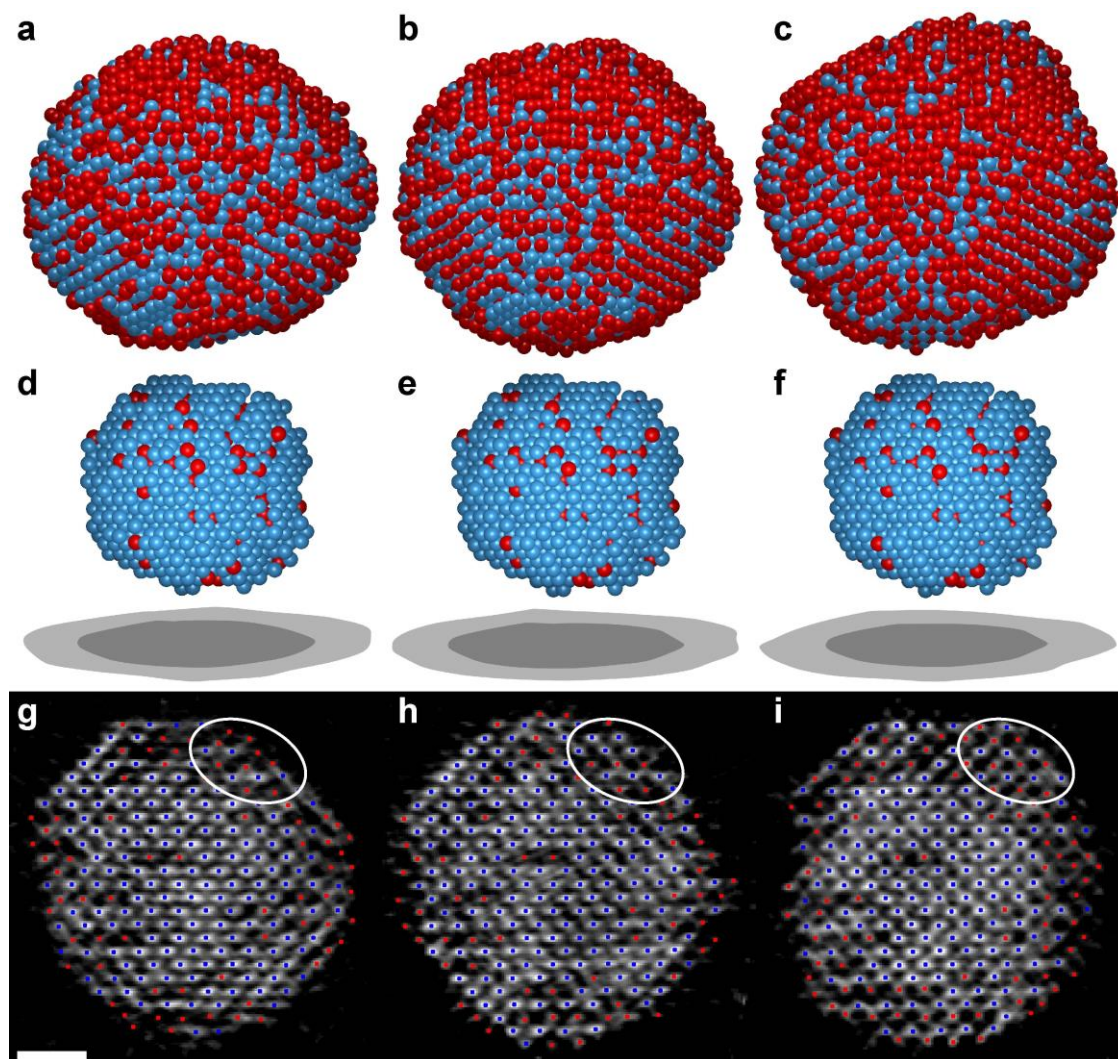
Figures and Figure legends

Figure 1 | Capturing 4D atomic motion with AET. **a-c,** 3D atomic models (Fe in red and Pt in blue) of an FePt nanoparticle with an accumulated annealing time of 9, 16 and 26 minutes, respectively. **d-f,** The Pt-rich core of the nanoparticle remained the same for the three annealing times. The light and dark grey projections show the whole nanoparticle and the core, respectively. **g-i**, The same internal atomic layer of the nanoparticle along the [010] direction at the three annealing times (Fe in red and Pt in blue), where a fraction of the surface and sub-surface atoms were re-arranged to form $L1_0$ phases (ellipses).
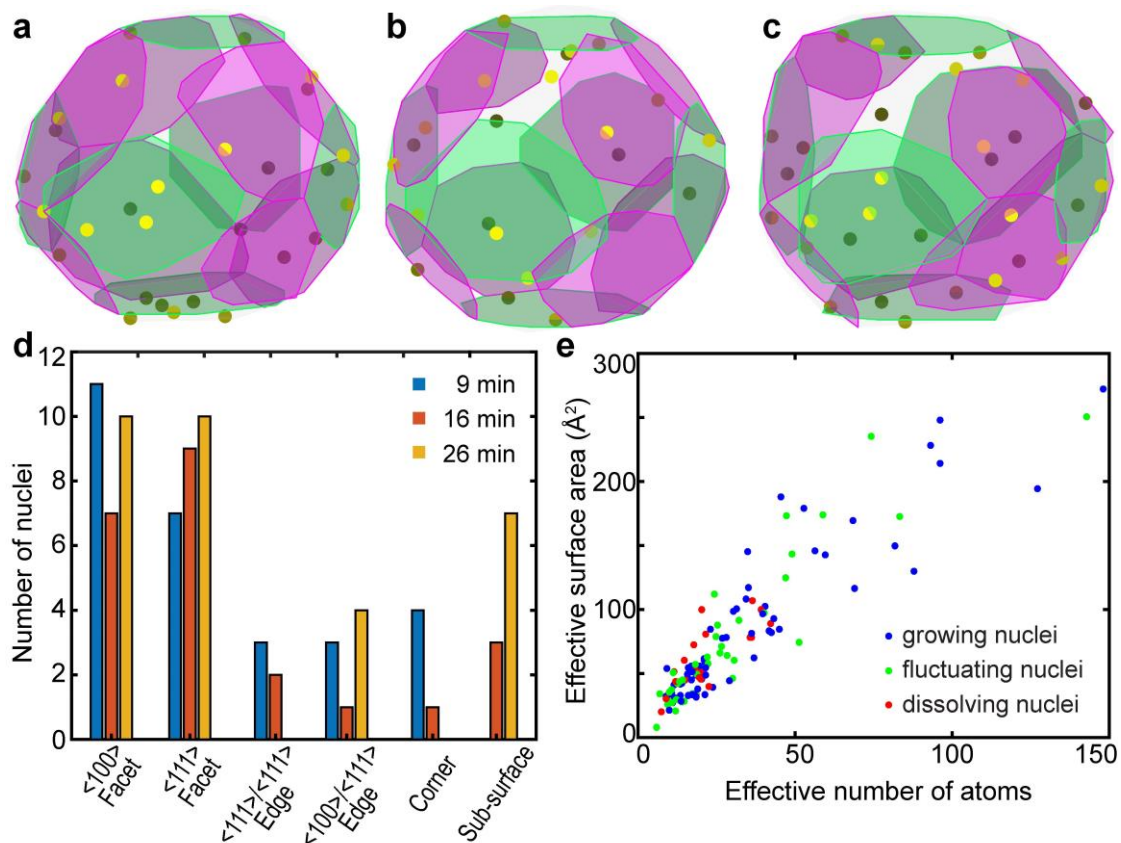
Figure 2 | Revealing heterogeneous nucleation sites. **a-c**, The distribution of the nucleation sites (circular dots) in particle 2 with an accumulated annealing time of 9, 16 and 26 minutes, respectively, where the lighter coloured dots are closer to the front side and the darker dots are closer to the back side of the nanoparticle. The <100> and <111> facets are in green and magenta, respectively. **d**, The histogram of the nucleation site distribution in particle 2, where most nucleation sites are located on the facets, edges or corners. **e**, A plot of the effective surface area vs. the effective number of atoms for all the nuclei in particles 2 and 3.
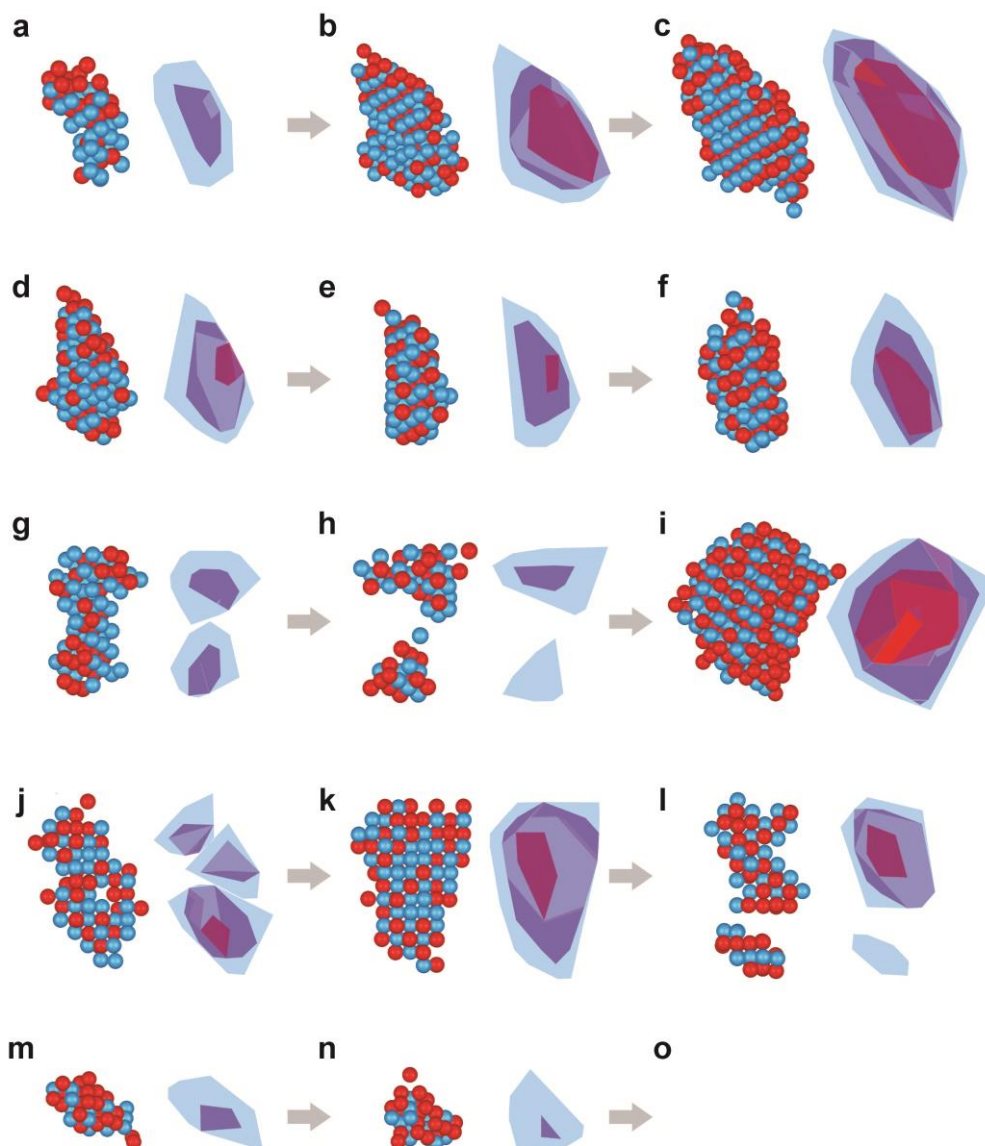
Figure 3 | Experimental observation of the same nuclei undergoing growth, fluctuation, dissolution, merging and/or division at 4D atomic resolution. a-c, A representative growing nucleus with an accumulated annealing time of 9, 16 and 26 minutes, respectively, where the atomic models show Fe (red) and Pt (blue) atoms with an order parameter $\geq$ 0.3 and the 3D contour maps show the distribution of an order parameter of 0.7 (red), 0.5 (purple) and 0.3 (light blue). **d-l**, Three representative fluctuating nuclei at three annealing times, including merging and dividing nuclei. **m-o**,

A representative dissolving nucleus at three annealing times, which dissolved at 26 minutes (**o**).
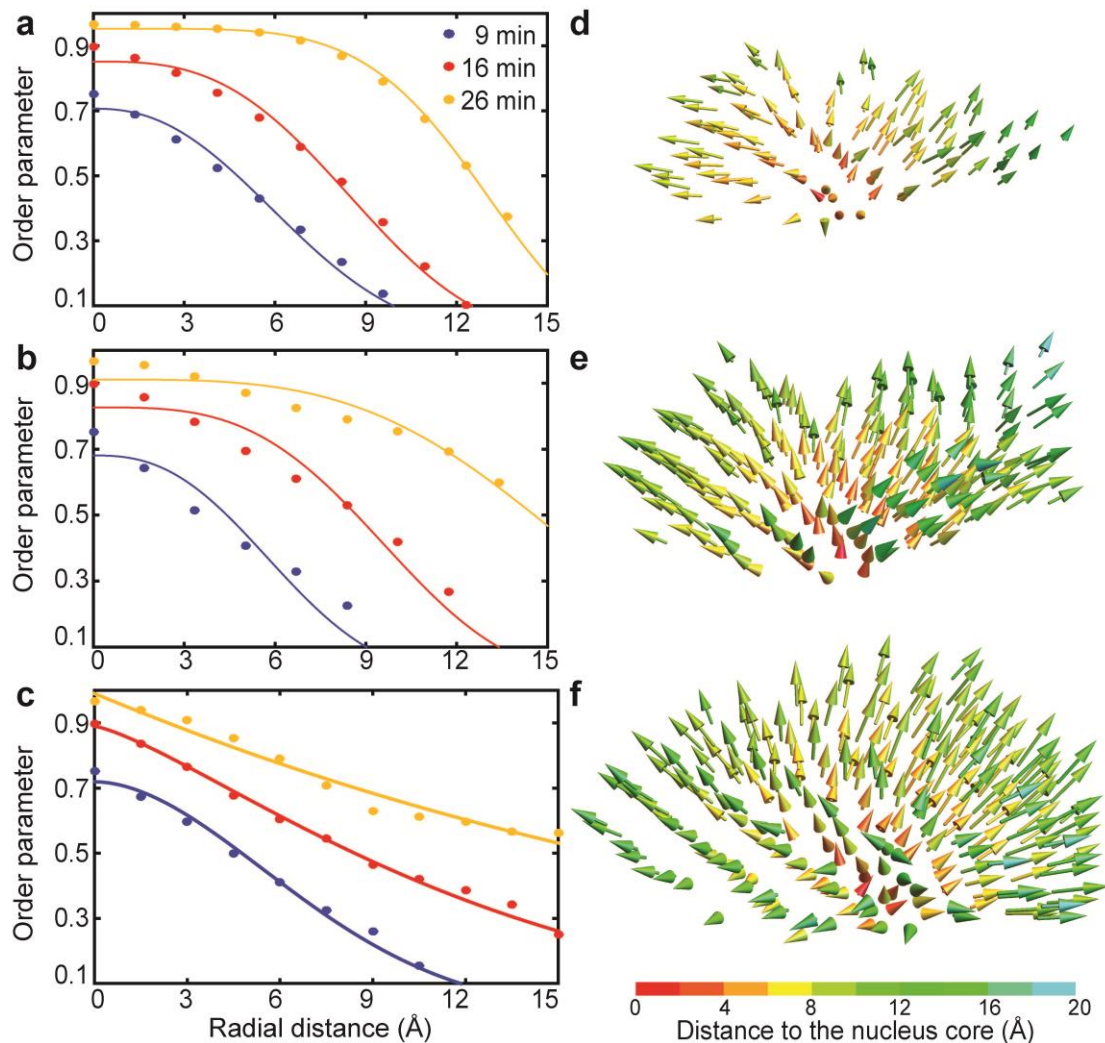

Figure 4 | The 3D distribution of the order parameter and its gradient inside a representative nucleus. **a-c**, The order parameter distribution of a growing nucleus (Fig. 3a-c) along the [110], [111] directions and with radial average, respectively, where the dots represent the experimental data and the curves are fitted with equation (1). **d-f**, The 3D OPG distribution of the nucleus at three annealing times, respectively, where the colours represent the distance to the nucleus core. With the growth of the nucleus, the OPG spreads out further along the radial direction. Note that the core is not at the centre of the nucleus.

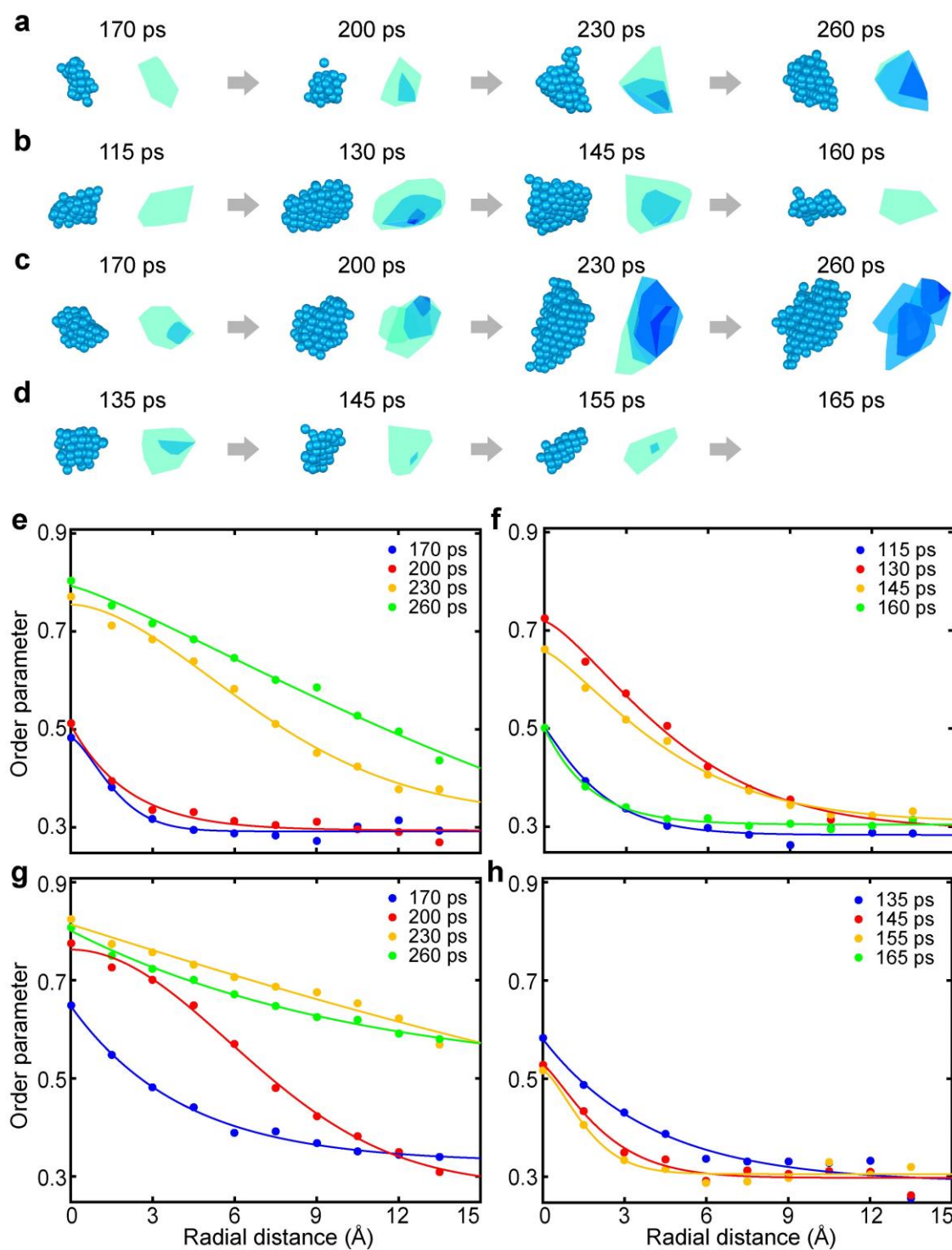**Figure 5 | MD simulations of nucleation dynamics in liquid-solid phase transitions of a Pt nanoparticle. a**, A representative growing nucleus, where the atomic models show the Pt atoms with an order parameter ≥ 0.3 and the 3D contour maps show the

distribution of an order parameter of 0.7 (dark blue), 0.5 (light blue) and 0.3 (cyan). **b** and **c**, Two representative fluctuating nuclei, where merging and dividing nuclei were observed in (**c**). **d**, A representative dissolving nucleus, which dissolved at 165 ps. **e-h**, Radial average order parameter distributions of the four nuclei shown in (**a-d**), respectively, where the dots were obtained by time-averaging ten consecutive MD snapshots with 1 ps time intervals and the curves are fitted with equation (1) using a constant background.

METHODS

Data acquisition. FePt nanoparticles were synthesized using the procedures published elsewhere[34]. After deposited on to 5-nm-thick silicon nitride membranes, the nanoparticles were annealed at 520 °C (below the melting temperature) for 9 minutes in vacuum. A set of tomographic tilt series were acquired from several FePt nanoparticles using the TEAM 0.5 microscope and the TEAM stage (Extended Data Table 1). Images were collected at 200 kV in annular dark-field scanning transmission electron microscopy (ADF-STEM) mode[28,35]. To minimize sample drift, four to five images per angle were measured with 3 μs dwell time. For the consistency check experiment, we took a second set of tomographic tilt series from the same nanoparticles under the identical experimental conditions. For the dynamics study experiment, we took the nanoparticles out of microscope and annealed them at 520 °C for additional 7 minutes. Based on the pattern of the nanoparticle distribution on the substrate, we identified the same nanoparticles and acquired a second set of tomographic tilt series from them. We then annealed the same nanoparticles at 520 °C for additional 10 minutes and acquired a 3rd set of tilt series. We chose three FePt nanoparticles to present in this work. Particle 1 was annealed for 9 minutes and two independent, sequential tilt series were acquired under the same experimental conditions. Particle 2 was annealed with an accumulated time of 9, 16 and 26 minutes and a tilt series was taken at each time. Particle 3 was annealed with an accumulated time of 9 and 16 minutes and a tilt series was acquired at each time. To monitor any potential structural changes induced by the electron beam, we took 0° projection images before, during and after the acquisition of each tilt series and ensured that no noticeable structural changes were observed during the data acquisition for particles 1, 2 and 3. The total electron dose of each tilt series for

particles 1, 2 and 3 was estimated to be between 7.6×10^5 e$^-$/Å^2 and 8.5×10^5 e$^-$/Å^2 (Extended Data Table 1), which is 5.6 to 6.3 times lower than that used in ref. 25.

Image post-processing, denoising and GENFIRE reconstructions. The four to five images acquired at each tilt angle were registered using normalized cross correlation[36] and then averaged. Linear stage drift at each tilt angle was estimated and corrected during the image registration. Scan distortion correction was also performed to correct for the imperfections in the calibration of the x- and y- scanning coils[23,25]. The experimental ADF-STEM images have mixed Poisson and Gaussian noise, and a sparse 3D transform-domain collaborative filtering[37] was applied to denoise the average image of each tilt angle. These post-processing and denoising methods have shown their robustness throughout other experimental data and multislice simulations[23,25,26].

After background subtraction and alignment, each tilt series was reconstructed using the GENFIRE algorithm[25,29]. From the initial 3D reconstruction, we applied the angular refinement routine implemented in GENFIRE to automatically correct the angular errors due to sample holder rotation and/or stage instability. After the automatic angular refinement, we manually applied additional angular correction and spatial alignment to minimize the distortions of Fourier space peak distributions and reduce the errors between the measured and calculated projections. After no further improvement can be made, we performed the final reconstruction of each tilt series using GENFIRE with the parameters shown in Extended Data Table 1.

Determination of 3D atomic coordinates and species. The 3D atomic coordinates and species of the nanoparticles were identified from the 3D reconstructions using the following procedure.

i) To enhance the tracing accuracy, we upsampled each 3D reconstruction by a factor of 3 using spline interpolation. All the local maxima were identified from the upsampled reconstruction.

ii) We implemented 3D polynomial fitting to localize the peak positions in each reconstruction, which generalizes a 2D method developed in particle tracking[38]. Starting from the highest-intensity local maximum peak, we cropped a ~$1.0 \times 1.0 \times 1.0$ Å^3 ($9 \times 9 \times 9$ voxel) volume with the selected local peak as the centre. We fit the volume with a 3D fourth-order polynomial function described elsewhere[38]. If a fitted peak position satisfied with a minimum distance constraint of 2 Å (i.e. the distance between two neighbouring atoms $\geq$ 2 Å), we listed it as a potential atom position. According to our multislice

simulations, the 3D polynomial fitting method is more accurate than 3D Gaussian fitting that has been used before[23,25].

iii) By applying the 3D polynomial fitting to all the identified local maxima, we obtained a list of potential atom positions. These positions were manually checked to correct for unidentified or misidentified atoms due to fitting failure or large chunk of connected intensity blobs from multiple atoms.

iv) We classified all the potential atoms into three different categories (non-atoms, potential Fe or Pt atoms) by applying an unbiased atom classification method described elsewhere[25]. With this classification procedure, we obtained an initial atomic model with 3D atomic coordinates and species from each 3D reconstruction.

v) Due to the missing wedge and experimental noise, there is local intensity variation in each 3D reconstruction. To further improve the atom classification accuracy, we performed local re-classification of the Fe and Pt atoms. For each atom in the initial atomic model, we drew a sphere with the atom as the centre and a radius of 6.76 Å. All the Fe and Pt atoms within the sphere were summed up to obtain an average Fe and Pt atom. The intensity distribution of the centre atom was compared with that of the average Fe and Pt atom. If the centre atom was closer to the average Fe than to the average Pt atom, it was assigned as an Fe atom, and vice versa. We iterated this process for all the atoms until the re-classification procedure was converged. Note that this process did not converge if the radius of the sphere was too small, and it became less effective if the radius was too large. By testing different radii, we found an optimal radius of 6.76 Å for this re-classification procedure.

Refinement of 3D atomic coordinates and species. We compared two atomic models of the same nanoparticle with each other. For particles 1 and 3, the two atomic models obtained from two experimental tilt series were compared. For particle 2, the 9-minute and 16-minute atomic models, and then the 16-minute and 26-minute atomic models were compared, respectively. We identified pairs of atoms (i.e. one atom from each model to form a pair), whose distance is within the radius of the Fe atom (1.4 Å). While the majority of the atom pairs have the same atomic species, there are a small percentage of atom pairs with different species. We developed the following atom flipping procedure to re-examine the atomic species of the small percentage of atom pairs.

i) An atom was randomly selected from the small percentage of atom pairs with different species. The projection intensities were calculated for all the tilt angles by flipping the selected atom (Fe

to Pt or Pt to Fe), and the error between the calculated and measured projections was estimated. As flipping a single atom only affects a small local region of a projection, we only considered the local region in this process to increase the computational speed.

ii) If the error was decreased after flipping, the flipped atomic species was updated in the model, otherwise the model was unchanged.

iii) Steps i) and ii) were repeated for all the small percentage of atom pairs and an updated atomic model was obtained. A global scale factor was computed to minimize the error between the measured and calculated projections from the updated model.

iv) Steps i)-iii) were iterated for all the small percentage of atom pairs until there was no change in the atomic species. This atom flipping method successfully converged for all datasets that we studied in this work.

From the updated atomic models, integrated intensity histograms for all atoms were plotted for each of the two atomic models in comparison. A double Gaussian function was fitted to the intensity histogram to identify obvious Fe atoms (integrated intensity smaller than the Fe atom peak), obvious Pt atoms (integrated intensity larger than Pt atom peak), and borderline atoms near the overlapping region of two Gaussians. We manually examined every borderline atom and its paired atom in the comparison model. If the paired common atom is classified as an obvious Fe or Pt atom, the atomic species of the borderline atom was re-classified to be consistent with its paired common atom.

After updating the chemical species for the atomic models in comparison, we refined the 3D atomic coordinates to minimize the error between the calculated and measured projections using the procedure described elsewhere[25]. During the refinement, we monitored both the total embedded-atom potentials and the root-mean-square deviation (RMSD) of the atomic coordinates between the atom pairs of the two models. For the RMSD calculation, appropriate affine transformations were applied to the atomic models to correct for remnant distortions. The iterative refinement process was terminated when a minimum RMSD was reached.

After finalizing the 3D coordinates, all the atomic species of unpaired atoms or paired atoms with different species in each model were refined again using steps i)-iv) described above. These atoms could be classified as Fe, Pt or non-atoms. To minimize misidentification, the atoms previously identified as obvious Pt atoms remained unaltered, and the atoms previously identified as obvious Fe atoms were

prohibited from being identified as Pt atoms. Using this refinement procedure, we obtained the final refinement results of the seven atomic models with 3D atomic coordinates and species (Extended Data Table 1).

Order parameter determination and nuclei identification. The short-range order parameters of the atomic sites in the final atomic models were calculated for all 16 possible ordered phases from the FePt fcc lattice[39,40] (four $FePt_3$ $L1_2$, four Fe_3Pt $L1_2$, six FePt $L1_0$, a Pt-rich A1, and a Fe-rich A1 phase). An order parameter S_j for a given phase j measures how many atomic sites in a set match the phase in question, normalized to the mean composition f_{all} of all atomic sites. We define f_j as the chemical composition of phase j. The fraction of atomic sites that match the chemical species between phase j and a disordered matrix of a given composition is computed by

$$f_{rand} = 2f_j f_{all} - f_j - f_{all} + 1 \quad . \qquad (2)$$

For a local measurement of the fraction of atomic sites matching with phase j defined as f, the normalized order parameter S_j is given by

$$S_j = \frac{f - f_{rand}}{1 - f_{rand}} = \frac{f - 2f_j f_{all} + f_j + f_{all} - 1}{f_j + f_{all} - 2f_j f_{all}} . \qquad (3)$$

This normalization step sets $S_j = 1$ for a perfectly chemically ordered set of atoms, and $S_j = 0$ if the fraction of atomic sites match phase j by chance in a fully chemically disordered structure. Note that $S_j < 0$ can occur for phases with anti-correlated site compositions. We then applied a Gaussian kernel with an optimized standard deviation of 0.75 fcc unit cells to prevent false positive grains at the disordered grain boundary. After determination of order parameters for all phases, every atom was assigned to one of the 16 phases based on its highest order parameter.

The nuclei in each atomic model were identified with the following procedure. For every atomic site, a sphere was drawn with the selected atom as the centre and a radius of 3.87 Å (one FePt fcc unit cell length). All the atomic sites inside the sphere were identified, which have the same ordered phase as that of the centre atom. If the highest order parameter atom inside the sphere is the centre atom, then the atom was defined as a core atom of a nucleus. Otherwise, the centre atom was tagged to be in the same nucleus as the highest order parameter atom, and a new sphere with the same radius and the highest order parameter atom as the centre was drawn to repeat the procedure until a nucleus core site was found. Applying this procedure to all atoms in each atomic model resulted in clusters of atoms with each cluster

having a core. A cluster with a minimum of 13 atoms and order parameter ≥ 0.3 was defined as a nucleus in this study. We chose a minimum of 13 atoms because an fcc cluster consists of a centre atom and 12 nearest-neighbour atoms. After identifying all the nuclei in the nanoparticles, we counted the number of atoms in the core of each nucleus. Using the criterion that the atoms in a nucleus core must be within top 5% of the maximum order parameter, we estimated that the core of each early stage nucleus has one to a few atoms.

Identification of common nuclei. The nucleation dynamics study was performed on particles 2 and 3, which have three and two annealing times, respectively. To identify the common nuclei for particles 2 and 3 at different annealing times, we used the following three criteria. First, a common nucleus can form, grow, merge, divide or dissolve at any annealing time. Second, if a common nucleus exists in at least two different annealing times, each must overlap with at least another nucleus with more than 50% of the volume of the smaller nucleus. Third, a common nucleus must not overlap with any non-common nuclei at different annealing times with more than 50% of the volume of the smaller one. Based on these three criteria, we found 33 common nuclei for particle 2, including 14 growing, 5 dissolving and 14 fluctuating nuclei. For particle 3, we found 25 common nuclei with 16 growing and 9 dissolving one. Since particle 3 has only two annealing times, it cannot be used to identify fluctuating nuclei. For all the nuclei in the two particles, we also performed an analysis of the tetragonal distortion of the $L1_0$ phase. We obtained the c/a ratio and calculated a weighted mean and standard deviation with the number of atoms of each nucleus as a weight factor. The weighted c/a ratios are 0.98 ± 0.02, 0.98 ± 0.03 and 0.97 ± 0.03 for the three different annealing times of particle 1, and 0.97 ± 0.02 and 0.98 ± 0.02 for the two different annealing times of particle 2, respectively, which agree with the c/a ratio of 0.96 for the bulk $L1_0$ phase.

MD simulations of heterogeneous and homogeneous nucleation in liquid-solid phase transitions of Pt. To further validate our experimental observations, we performed MD simulations on two Pt nanoparticles and a Pt bulk system using the LAMMPS package[31]. We first used an embedded-atom method potential to simulate a Pt nanoparticle of 32,000 atoms[41], which was put in a much larger box so that it does not interact with its periodic images. The nanoparticle was melt and equilibrated at 2,500 K and then quenched to room temperature with a cooling rate of 1 K·ps^{-1}. The heterogeneous crystal nucleation initiates at 1,050 K in the supercooling region. The potential energy significantly drops when crystallization initiates. To examine the detailed nucleation processes, we selected the cooling snapshot at

1,100 K and performed fixed temperature simulations at the 1,100 K using the NVT ensemble (constant number of particle, constant volume and constant temperature). Since the system was in supercooling region, the crystallization started at ~150 ps and ended at ~300 ps.

To cross-validate the MD results, we simulated another Pt nanoparticle of 13,500 atoms in the canonical (NVT) ensemble in LAMMPS using the interface force field as the interatomic potential[42]. The nanoparticle was melt at 2,750 K for 300 and the temperature was lowered to 2,000 K for 200 ps. At this temperature the Pt nanodroplet showed no nucleation. The nanodroplet was then quenched to 1,650 K for 1 ns with a cooling rate of 1.65 $K \cdot ps^{-1}$. During this cooling period, nucleation and liquid-solid phase transitions of Pt were induced and observed. Coordinates were recorded every 1 ps during this part of the simulation and used to analyse the in-situ change of the order parameter and atomic displacements during the nucleation process.

In addition to heterogeneous nucleation, we also performed MD simulations of homogeneous nucleation using a bulk Pt system. An embedded-atom method potential was used to simulate 32,000 Pt atoms[41] and periodic boundary conditions were applied along three directions to eliminate the surface effects. The system was equilibrated at 2,500 K and quenched to room temperature with a cooling rate of 1 $K \cdot ps^{-1}$. In contrast to the Pt nanodroplet, the bulk system crystallized at ~750 K during quench process, which is lower in temperature than the heterogeneous nucleation process. This is because the homogeneous system has much less nucleation sites than the nanodroplet. The nucleation process was examined at a fixed temperature of 800 K using the NPT ensemble (constant number of particle, constant pressure and constant temperature). The crystallization initiated in the first few picoseconds and ended at ~200 picoseconds.

Order parameter definition and nuclei identification for the MD simulation results. The order parameters of the Pt atoms in the MD simulations were calculated using local bond-orientation order parameter method[32,33,43]. The Q_4 and Q_6 order parameters were calculated up to the second shell with the shell radius of 3.8 Å as described elsewhere[43]. The order parameter was normalized between 0 and 1 where 0 corresponds to $Q_4 = Q_6 = 0$ and 1 represents a perfect Pt fcc structure. To identify the nuclei formed during the heterogeneous and homogeneous nucleation, we applied the same method described above with a 4-Å-radius sphere and a minimum of 31 atoms. Common nuclei at different time points were also identified using the same method described above. Note that the local bond-orientation order parameter

has been previously used to study crystallization with computer simulations[44,45].

To examine the 3D shapes of the nuclei in the MD simulations of heterogeneous and homogeneous nucleation, we calculated the sphericity of the nuclei in the crystallization of Pt (Extended Data Fig. 4i and j). The distribution of the sphericity of the nuclei in the MD simulations is in good agreement with that of the experimental data (Extended Data Fig. 4h). In particular, for homogeneous nucleation we used the embedded-atom method potential with the periodic boundary condition to simulate a bulk Pt system undergoing liquid-solid phase transitions. This system does not have a surface constraint for nucleation, but its early stage nuclei remain nonspherical (Extended Data Fig. 4j), which is consistent with our experimental observations (Extended Data Fig. 4h).

34. Xu, C. *et al.* FePt Nanoparticles as an Fe Reservoir for Controlled Fe Release and Tumor Inhibition. *J. Am. Chem. Soc.* **131,** 15346–15351 (2009).

35. Muller, D. A. Structure and bonding at the atomic scale by scanning transmission electron microscopy. *Nat. Mater.* **8**, 263–270 (2009).

36. Lewis, J. P. Fast Normalized Cross-Correlation. *Vis. Interface* **95,** 120–123 (1995).

37. Dabov, K., Foi, A., Katkovnik, V. & Egiazarian, K. Image Denoising by Sparse 3-D Transform-Domain Collaborative Filtering. *IEEE Trans. Image Process.* **16,** 2080–2095 (2007).

38. Rogers, S. S., Waigh, T. A., Zhao, X. & Lu, J. R. Precise particle tracking against a complicated background: polynomial fitting with Gaussian weight. *Phys. Biol.* **4,** 220–227 (2007).

39. Finel, A., Mazauric, V. & Ducastelle, F. Theoretical study of antiphase boundaries in fcc alloys. *Phys. Rev. Lett.* **65**, 1016–1019 (1990).

40. Müller, M. & Albe, K. Lattice Monte Carlo simulations of FePt nanoparticles: influence of size, composition, and surface segregation on order-disorder phenomena. *Phys. Rev. B* **72**, 094203 (2005).

41. Zhou, X. W., Johnson, R. A. & Wadley, H. N. G. Misfit-energy-increasing dislocations in vapor-deposited CoFe/NiFe multilayers. *Phys. Rev. B* **69,** 144113 (2004).

42. Heinz, H., Vaia, R. A., Farmer, B. L. & Naik, R. R. Accurate Simulation of Surfaces and Interfaces of Face-Centered Cubic Metals Using 12−6 and 9−6 Lennard-Jones Potentials. *J. Phys. Chem. C* **112,** 17281–17290 (2008).

43. Wang, Y., Teitel, S. & Dellago, C. Melting of icosahedral gold nanoclusters from molecular

dynamics simulations. *J. Chem. Phys.* **122,** 214722 (2005).

44. Auer, S. & Frenkel, D. Numerical prediction of absolute crystallization rates in hard-sphere colloids. *J. Chem. Phys.* **120,** 3015–3029 (2004).

45. Russo, J. & Tanaka, H. The microscopic pathway to crystallization in supercooled liquids. *Sci. Rep.* **2,** 505 (2012).

Data availability. All the raw and processed experimental data can be freely downloaded at www.physics.ucla.edu/research/imaging/nucleation. All the seven experimental atomic models with 3D coordinates of particles 1, 2 and 3 have been deposited in the Materials Data Bank (MDB, www.materialsdatabank.org) with their MDB IDs provided in Extended Data Table 1.

Code availability. All the Matlab source codes for image reconstruction and data analysis of this work are freely available at www.physics.ucla.edu/research/imaging/nucleation.